Mapping and Modeling the Nanomechanics of Bare and Protein-Coated Lipid Nanotubes

Guillaume Lamour,[1,*] Antoine Allard,[1,2] Juan Pelta,[1] Sid Labdi,[1] Martin Lenz,[3] and Clément Campillo[1,†]

[1]*LAMBE, Université d'Evry, CNRS, CEA, Université Paris-Saclay, 91025, Evry-Courcouronnes, France*
[2]*Physico Chimie Curie, CNRS UMR168, Institut Curie, F-75005 Paris, France*
[3]*LPTMS, CNRS, Université Paris-Sud, Université Paris-Saclay, 91405 Orsay, France*

(Received 13 September 2019; revised manuscript received 22 December 2019; accepted 10 January 2020; published 11 February 2020)

Membrane nanotubes are continuously assembled and disassembled by the cell to generate and dispatch transport vesicles, for instance, in endocytosis. While these processes crucially involve the ill-understood local mechanics of the nanotube, existing micromanipulation assays only give access to its global mechanical properties. Here we develop a new platform to study this local mechanics using atomic force microscopy (AFM). On a single coverslip we quickly generate millions of substrate-bound nanotubes, out of which dozens can be imaged by AFM in a single experiment. A full theoretical description of the AFM tip-membrane interaction allows us to accurately relate AFM measurements of the nanotube heights, widths, and rigidities to the membrane bending rigidity and tension, thus demonstrating our assay as an accurate probe of nanotube mechanics. We reveal a universal relationship between nanotube height and rigidity, which is unaffected by the specific conditions of attachment to the substrate. Moreover, we show that the parabolic shape of force-displacement curves results from thermal fluctuations of the membrane that collides intermittently with the AFM tip. We also show that membrane nanotubes can exhibit high resilience against extreme lateral compression. Finally, we mimic *in vivo* actin polymerization on nanotubes and use AFM to assess the induced changes in nanotube physical properties. Our assay may help unravel the local mechanics of membrane-protein interactions, including membrane remodeling in nanotube scission and vesicle formation.

DOI: 10.1103/PhysRevX.10.011031

Subject Areas: Biological Physics, Soft Matter

I. INTRODUCTION

Exchanges of matter between and within living cells are strongly constrained by their membrane, a thin lipid bilayer that delimits their outer envelope as well as their inner compartments. To accommodate these exchanges, the cell often remodels this membrane into hollow, single-walled cylindrical nanotubes with a diameter of 20–200 nm. *In vivo*, these nanotubes mediate long-distance intercellular communication and organelle transfer [1,2]. Within the cell itself, they serve as precursors for vesicle formation in intracellular transport or endocytosis [3] and form mostly from the relatively flat membrane of the endoplasmic reticulum [4] and Golgi apparatus [5]. While the associated lipid membrane deformations are mediated by many proteins [6–8] including the actomyosin cytoskeleton [9–12], the local mechanisms through which proteins mechanically remodel nanotubes are still unclear.

In addition to their functional role in the cell, nanotubes also have great potential as a diagnostic tool for human diseases [13], and as building blocks for nanotechnological applications, e.g., soft nanofluidics networks [14–16]. These devices typically rely on nanotubes reconstituted through either a biochemical or a physical approach. In the former, proteins such as bin-amphiphysin-Rvs (BAR) [17,18] or microtubules with kinesin motors [19] associate with the membrane to create invaginations that result in nanotube formation. In the latter approach, lipid bilayers deposited on a substrate [20] or stored in a giant vesicle [16,21–23] are directly deformed using optical tweezers [22,23], a micropipette [16], or hydrodynamic flow [20,21].

Studies of the mechanical properties of membrane nanotubes have until now largely consisted of directly probing them with optical tweezers and micropipettes. While these techniques allow for a fine, piconewton-scale control of the applied force, they are limited to studying only one nanotube at a time. Moreover, they provide only a coarse, micrometer-scale spatial resolution, and are thus best suited to studies of the global mechanics of the nanotube. By contrast, here we use hydrodynamic flow to generate millions of supported nanotubes on the same

*Corresponding author.
guillaume.lamour@univ-evry.fr
†Corresponding author.
clement.campillo@univ-evry.fr

cover slip [20], and then locally characterize dozens of them in a single atomic force microscopy (AFM) experiment.

AFM has been previously used to probe membrane structures [24–26], including nanotubes with large diameters (≈500 nm) and stiff crystalline multilayer walls [27], or nanotubes rigidified by a protein coat [28]. However, the imaging of thin, soft membrane nanotubes analogous to those at work in the cell has remained elusive. Here we meet this challenge by firmly attaching the nanotubes to a modified glass surface and using an imaging protocol whereby the AFM tip always approaches the nanotubes vertically, which avoids damaging them. This strategy allows us to resolve the local mechanics of a nanotube with a spatial resolution on the order of a few nanometers. Combining our data with a theoretical description of the membrane mechanics, we locally extract the nanotube tension and bending rigidity, which have a crucial role in shaping membranes [29], and thence in orchestrating morphological transitions. Our theoretical model also predicts a universal relationship between nanotube height and rigidity that we verify experimentally. Moreover, this contact mechanics model shines light on the role of local membrane fluctuations in modulating the nanotube mechanical response to the displacement induced by the AFM tip. Finally, we demonstrate the potential of our technique to elucidate membrane-protein interactions by polymerizing a soft, diffuse actin coat with a mesh size of 30–150 nm comparable to physiological values [30,31] onto the nanotubes, and by characterizing the associated modification of the nanotube morphology and rigidity. Taken together, these results demonstrate the ability of our assay to quantitatively monitor the mechanics of nanotubes at the scale of single proteins with a high throughput, as well as their reshaping by a wide range of biomolecules.

II. AFM MAPPING

AFM allows direct mechanical probing of surface-bound nanotubes.—We generate nanotubes using hydrodynamic flow and firmly attach them to a streptavidin-coated glass surface using biotinylated lipids, thus allowing them to stay in place throughout the rest of the experiment [Fig. 1(a); see details in Sec. VI]. We carry out AFM imaging using the Quantitative Imaging™ (QI) mode [Figs. 1(b) and 1(c)]. In this mode, the AFM always moves its tip away from the sample before moving laterally, which prevents shear damage to our soft nanotubes. It then progressively moves the tip vertically toward the sample, thus collecting a full force-distance curve for each pixel in the image. As the resulting force-displacement curves have a parabolic shape and no hysteresis [Figs. 2(b) and 3], we fit the dependence of the force f on the indentation depth δ through $f = K\delta^2$ for $\delta > 0$, where the parameter K characterizes the local rigidity of the sample and where we use the location of the $\delta = 0$ point of contact to determine the local height h of the nanotube. We first use this method on nanotubes made of a relatively rigid lipid mixture of sphingomyelin and cholesterol (SMC) (at 1∶1 molar ratio), yielding a spatial map of the rigidity K shown in Fig. 1(c). The edges of the nanotube are well resolved in this representation, as shown by the high-resolution, sharp contours apparent in the figure. Our heights and width measurements are moreover very homogeneous across the image, demonstrating reproducible AFM imaging and mechanical characterization of bare nanotubes with nanoscale resolution.

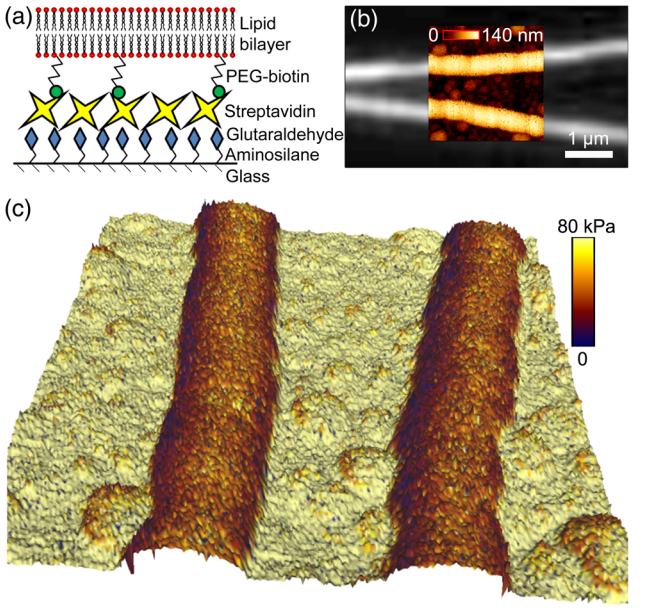

FIG. 1. Nanomechanical mapping of membrane nanotubes. (a) Schematic illustrating the specific attachment of the nanotube lipids to the functionalized glass surface (not to scale). (b) AFM topography image (yellow and brown) of two nanotubes superimposed on the fluorescence image (gray) displaying the same nanotubes. AFM height scale (0–140 nm) displays high and low regions as bright and dark, respectively. (c) AFM mapping of the rigidity (colors) superimposed on the 3D topographic representation of the nanotube heights. Colors show stiff and soft materials as bright and dark, respectively. Both nanotubes have a rigidity of 38 ± 14 kPa.

To test the reproducibility of our rigidity measurements, we position the AFM tip over a SMC nanotube and collect hundreds of successive force-displacement curves at a single point of contact [Fig. 2(a)]. We fit the value of the rigidity K to each curve [Fig. 2(b)]. We measure $K = 37 \pm 8$ kPa independently of indentation speed across 2 orders of magnitude, from 0.1 up to 20 μm/s [Fig. 2(c)]. Consistent with the absence of hysteresis between our approach and retraction curves, this confirms that the membrane mechanical response is purely elastic under our standard imaging conditions (setpoint force ≤ 110 pN; see Sec. VI).

Nanotube height and rigidity are inversely correlated.—While conducting multiple successive indentations at a single location, we find that the altitude of the contact point

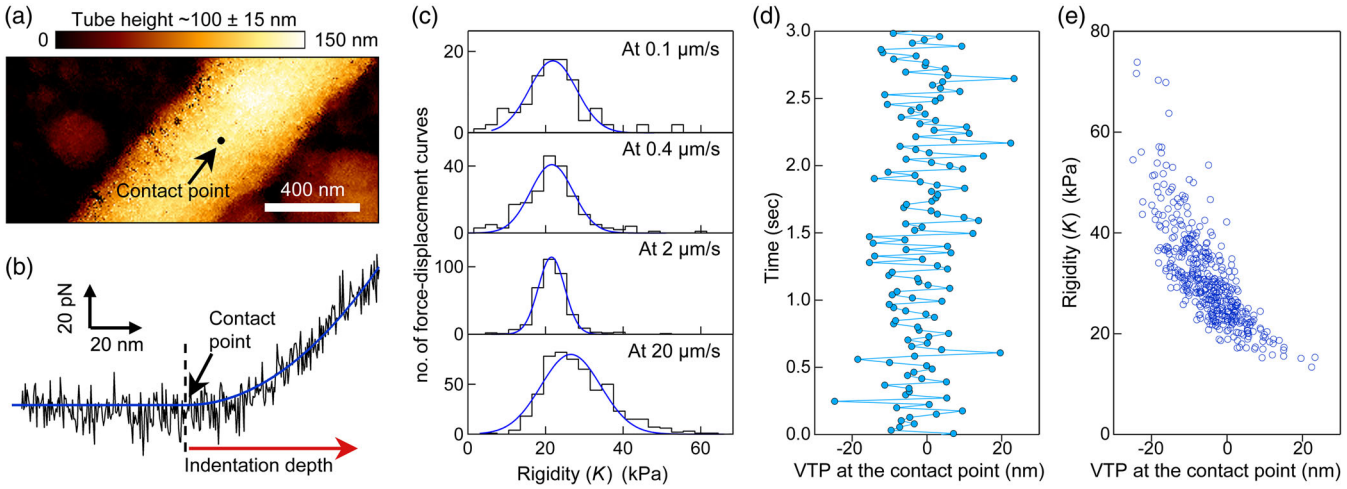

FIG. 2. Multiple force-distance curves collected at a single point of contact on a nanotube. (a) AFM image of a SMC nanotube. The arrow points to where all the force curves analyzed in (b)–(e) are recorded. (b) Example of a force curve recorded at a speed of 2 μm/s. The blue line is the result of fitting the equation $f = K\delta^2$ to the data and returns the rigidity (here $K = 24$ kPa). (c) Distribution of K derived from force curves collected at different indentation speeds. Blue lines are Gaussian fits to the data. (d) Time versus vertical tip position (VTP), which indicates the height at which the AFM tip contacts the nanotube during its downward vertical movement. (e) K plotted as a function of the VTP. In this graph K is derived from force curves collected at a speed of 20 $\mu m/s$ and it corresponds to the data displayed in (d) and in the bottom graph in (c).

fluctuates from one indentation to the next [Fig. 2(d)] over a range of ±20 nm (≃20% of the average nanotube height). As the height varies, so does the rigidity K [Fig. 2(c)], and we observe that the taller the nanotube, the softer it tends to be [Fig. 2(e)]. We attribute this change to variations in the area of the nanotube adhered to the surface over successive indentations. Because of the limited number of lipids available, a more adhered nanotube tends to be flatter. It is moreover put under a larger tension as the adhesion pulls the nanotube down, which makes it appear stiffer to the AFM indentation.

Softer lipids yield smaller nanotubes.—To assess the dependence of the nanotube morphology and rigidity on its lipid composition, we collect data on many nanotubes and supplement them with nanotubes formed from the softer 1,2-dioleoyl-sn-glycero-3-phosphocholine lipid (DOPC) [Fig. 4(a)]. On average, DOPC form much smaller nanotubes than SMC [Fig. 4(b)]. DOPC nanotubes have heights and widths of 40–80 and 40–140 nm, respectively, versus 80–180 and 90–410 nm, respectively, for SMC nanotubes. Consistent with their larger sizes, cross-sectional areas are 5 times higher in SMC than in DOPC nanotubes. In contrast with their different sizes, DOPC and SMC nanotubes exhibit similar aspect ratios (width over height), meaning that neither looks significantly flatter than the other.

Assessing the actual height and width of a nanotube.—As nanotubes are soft objects attached to the modified glass surface by flexible 13-nm-long polyethylene glycol (PEG) linkers, we assess whether they might slide sideways under increasing AFM forces, which could bias our mechanical and morphological measurements. We first focus on measurements of the nanotube height at the center of their cross section. Increasing the force from 0 to 2 pN and then to 50 pN results in a monotonic decrease of the apparent nanotube height, suggesting that the nanotube remains in place under vertical compression [Fig. 4(a)]. In a case where we increase this force to 400 pN, we find that the nanotube remains under the AFM tip all the way down to the point where its thickness should be equal to that of two stacked lipid bilayers [see Fig. 3(c)], confirming that the nanotube remains firmly in place regardless of the value of the vertically exerted AFM force. This last measurement additionally provides an independent measure of the nanotube height that is consistent with our previous estimations. It also indicates that nanotubes can be highly resilient as they can sustain high levels of deformation without rupturing.

Turning to measurements of the nanotube widths, we find that maps acquired at a 2 pN force yield larger apparent nanotube widths than those acquired at 0 pN and at 50 pN [Fig. 4(b)]. It results from the flexibility of the nanotubes and PEG linkers, and from the fact that the AFM tip pushes nanotubes sideways when indenting them in their peripheral regions (see Sec. VI). We conclude that using the 2-pN-force height map of a nanotube supplies the most accurate estimation of the nanotube width, as it appears to be systematically underestimated in both 0 and 50 pN height maps.

III. MODEL

Nanotube rigidity gives direct access to the membrane mechanical parameters.—To understand the wide spread of our rigidity measurements for nanotubes of different

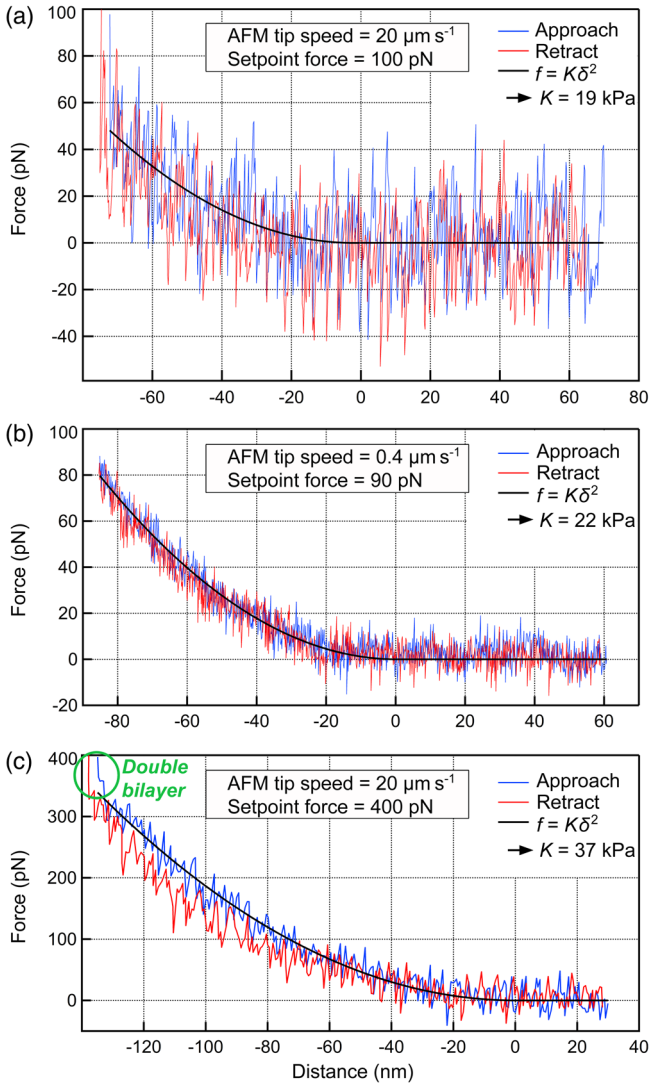

FIG. 3. High resilience of SMC nanotubes. (a) Force-distance curves collected at a speed of 20 μm/s and (b) at a speed of 0.4 μm/s on the same nanotube. Note that in both graphs K are similar, although the amount of thermal noise is clearly higher at higher speed. (c) Force-distance curves collected on another nanotube (height 130 ± 10 nm) with a high setpoint force of 400 pN. At such high force, the nanotube is fully compressed (i.e., maximum indentation depth similar to nanotube height) and the indenter pushes on a double bilayer, as indicated by the sudden increase in force when indentation depth reaches ~130 nm (circle). N.B., in all graphs, the approach and retract curves overlap, at least for forces under 100 pN (i.e., maximum setpoint force typically used for imaging), indicating no hysteresis and thence purely elastic behavior. Furthermore, as the tip retracts from the nanotube, the nanotube does not maintain contact with the tip, indicating the absence of (detectable) nonspecific adhesion between the tip and the nanotube.

heights [from 3 to 300 kPa, displayed in Fig. 5(a)] and quantitatively extract the membrane mechanical parameters from these measurements, we derive a mechanical model of our indentation geometry. Our model considers a flattened nanotube (which is consistent with our AFM images) made of an infinitely thin membrane with bending rigidity κ and tension σ [Fig. 5(b)] and infers their values from measurements of the nanotube thickness h and rigidity K.

Approximating the two rounded rims of the nanotube as half cylinders and applying force balance, we find that the diameter of the cylinders, which is also equal to the overall thickness of the flattened nanotube, is given by

$$h = \sqrt{2\kappa/\sigma}. \tag{1}$$

This relation quantitatively expresses the previously discussed notion that flatter nanotubes (h small) are tenser (σ large). To further express the AFM-measured rigidity K as a function of κ and σ, we approximate the flat region at the top of the nanotube by a horizontal membrane patch of lateral size w. Indenting a rounded AFM tip at the center of the patch induces a membrane deformation for which we derive an analytical expression (see the Appendix). For small indentation depths δ and large patch size w, the force f exerted on the membrane is given by

$$f = \begin{cases} 0 & \text{if } \delta \leq 0 \\ \dfrac{2\pi\sigma\delta}{\gamma + \ln\left(\frac{w}{2}\sqrt{\frac{\sigma}{\kappa}}\right)} & \text{if } \delta > 0, \end{cases} \tag{2}$$

where $\gamma \simeq 0.577$ is the Euler gamma constant. For large w, this expression shows a very weak (logarithmic) dependence on w and κ, implying that the elastic response of the nanotube to AFM indentation is dominated by the tension σ of its membrane.

Equation (2), which derives from an assumption of mechanical equilibrium, displays a linear relationship between f and δ that contrasts with the rounded shape of the force curves of Figs. 2(b) and 3. This apparent inconsistency is resolved by realizing that thermal fluctuations play a crucial role at the scale of the nanotube, and imply that contact between the indenter and the membrane does not occur discontinuously at $\delta = 0$, but that the rapidly fluctuating membrane collides with the indenter before proper contact is established, implying a rounding off of the linear relationship expressed by Eq. (2). By computing the effect of these fluctuations in the Appendix, we find a functional form for the force-displacement relation given by

$$f \propto \sqrt{\frac{2kk_BT}{\pi}} \frac{e^{-k\delta^2/2k_BT}}{\mathrm{erfc}(\delta\sqrt{k/2k_BT})}, \tag{3}$$

which gives a similar fluctuation-induced rounding as was proposed in models of actin filaments interacting with a fluctuating membrane [34], and where $k = 2\pi\sigma/\{\gamma + \ln[(w/2)(\sqrt{\sigma/\kappa})]\}$ and erfc is the complementary error function [35]. We further show that over the relevant parameter range, this expression is well approximated by the half-parabola used to fit our experimental data provided that

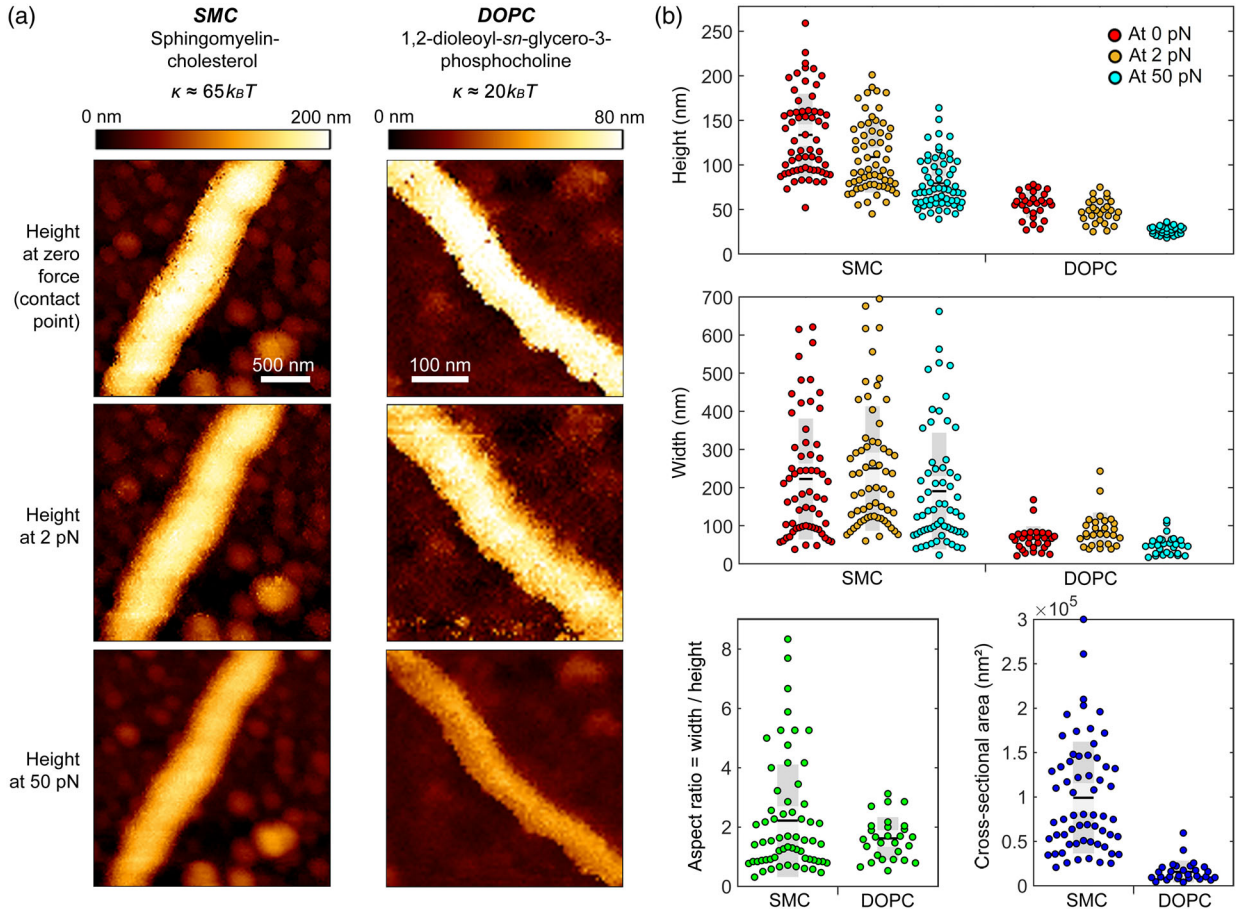

FIG. 4. High-throughput probing of nanotube morphologies by AFM. (a) Examples of QI mode AFM images collected for nanotubes with two different lipid compositions, resulting in different rigidities. The bending rigidities κ listed here were independently determined for lipid bilayers in vesicles at room temperature [32,33]. Force curves were collected, and the heights measured at forces of 0, 2, and 50 pN are reported in separate images. (b) From top to bottom: heights, widths, aspect ratios, cross-sectional areas of all nanotubes ($N = 62$ for SMC and $N = 28$ for DOPC). Aspect ratios and cross-sectional areas are calculated using the height at 0 pN and the width at 2 pN (see Sec. VI for details). Black horizontal lines and gray boxes represent the mean plus or minus 1 standard deviation.

$$K = \alpha \frac{\kappa^{3/2}}{\sqrt{k_B T} h^3}, \tag{4}$$

where Eq. (1) was used to eliminate σ and where the value of the numerical prefactor $\alpha \simeq 22$ is predicted by the detailed theory for our experimental regime (see the Appendix).

To validate this mechanical model, we first assess the predicted power-law dependence between K and h, and find that it indeed provides a good description of the data of Fig. 5(a) for each type of lipid used. To further validate the predicted dependence on the membrane rigidity, we use the known value of the bending rigidity for each lipid type [32,33] and plot the rescaled rigidity $K/\kappa^{3/2}$ as a function of nanotube height [Fig. 5(c)]. Consistent with our model, it falls onto a master curve that is independent of the type of lipid used, indicating that our model is an excellent predictor of the nanotube rigidity. Having established the reliability of our model, we conclude that the following equations, obtained by combining Eqs. (1) and (4), provide a direct prescription to compute the membrane tension and bending rigidity from AFM measurements of the height and rigidity of a flattened nanotube:

$$\sigma = \frac{2}{\alpha^{2/3}} (k_B T)^{1/3} K^{2/3}, \tag{5a}$$

$$\kappa = \frac{h^2}{\alpha^{2/3}} (k_B T)^{1/3} K^{2/3}, \tag{5b}$$

Our rigidity measurements, which spread from 3 to 300 kPa, thus yield membrane tension of 0.008–0.18 mN/m (0.038 ± 0.027 mN/m for SMC and 0.079 ± 0.049 mN/m for DOPC). These values compare well to the characteristic tensions of 0.01–0.3 mN/m measured in the plasma membranes of many distinct cells [36,37]. Applying Eq. (5) to calculate the average bending rigidities of our nanotubes, we find $64 \pm 30 k_B T$ and $23 \pm 5 k_B T$ for SMC and DOPC, respectively. Again, these values compare very well to the literature values (i.e., $65 k_B T$ for SMC and

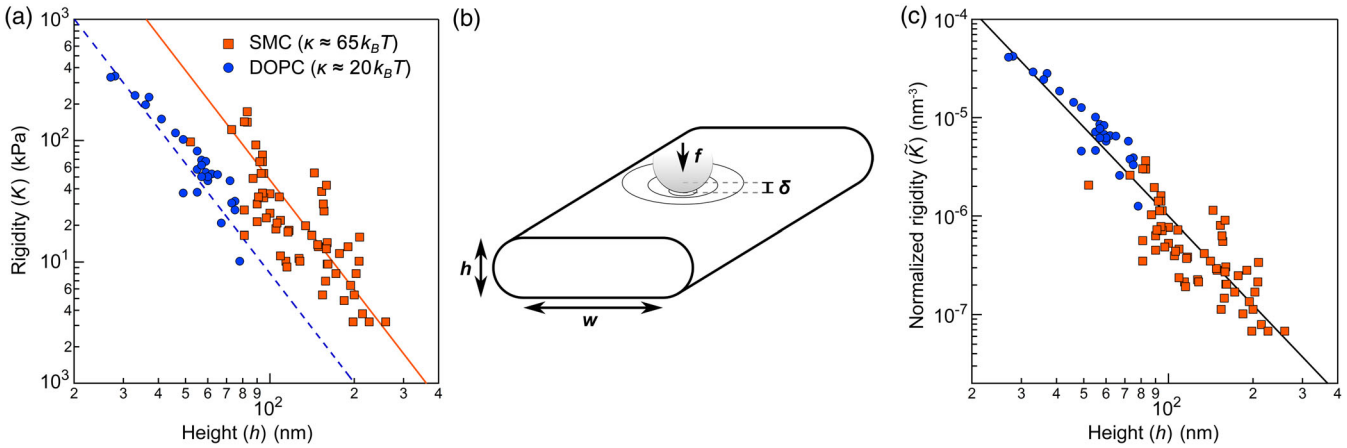

FIG. 5. Nanomechanical properties of membrane nanotubes. (a) Rigidity K plotted against the AFM height h. Each data point represents one nanotube. Lines display the model with no adjustable parameter $K = 22\,\kappa^{3/2}(k_BT)^{-1/2}h^{-3}$, with κ the bending rigidity of the membrane (see text for details). (b) Schematics of the flattened nanotube and indentation geometry considered in our model. f is the force exerted on the membrane by the AFM tip, δ the indentation depth, h and w the nanotube height and width, respectively. (c) Normalized rigidity $\tilde{K} = K/[22\,\kappa^{3/2}(k_BT)^{-1/2}]$ versus height for all nanotubes. Data points from the two sets of nanotubes (SMC and DOPC) collapse on the same master curve (black line), as predicted by the model.

$20k_BT$ for DOPC [32,33]). The rigidity estimates show a rather large dispersion, especially for SMC nanotubes. The dispersion stems from two related effects. First, nanotube height fluctuates [see Fig. 2(e)], which produces an uncertainty on the order of 30%. Second, softer nanotubes might undergo more fluctuations, which would be consistent with the higher dispersion observed for taller nanotubes (see Fig. 5).

IV. COATING PROTEINS ON NANOTUBES

Nanotubes can serve as a substrate for actin polymerization.—To mimic the coating of membrane nanotubes by networks of semiflexible filaments composed of the polymerized protein actin *in vivo*, we introduce a fusion protein called SpVCA that binds to the biotinylated membrane through its streptavidin domain [Fig. 1(a)] along with the actin-associated protein complex Arp2/3. Together, these proteins initiate the polymerization of actin at the nanotube surface [38] (see Sec. VI for details). Figure 6(a) indeed shows that green-labeled actin polymerizes on DOPC nanotubes, whereas control samples without actin [Fig. 6(b)] or with actin but without the activators (not shown) display no green fluorescence. Background noise is relatively low in all cases, showing that actin polymerizes mostly on the nanotubes and not on the underlying substrate.

Actin coats around membrane nanotubes can be directly probed by AFM.—To reveal how coating a nanotube with an actin gel changes its nanomechanics and morphology, we first use AFM to characterize 12 SMC nanotubes at the same locations before and after actin polymerization [Figs. 7(a)–7(c)]. We find that actin polymerization generally results in an increase of the nanotube apparent width,

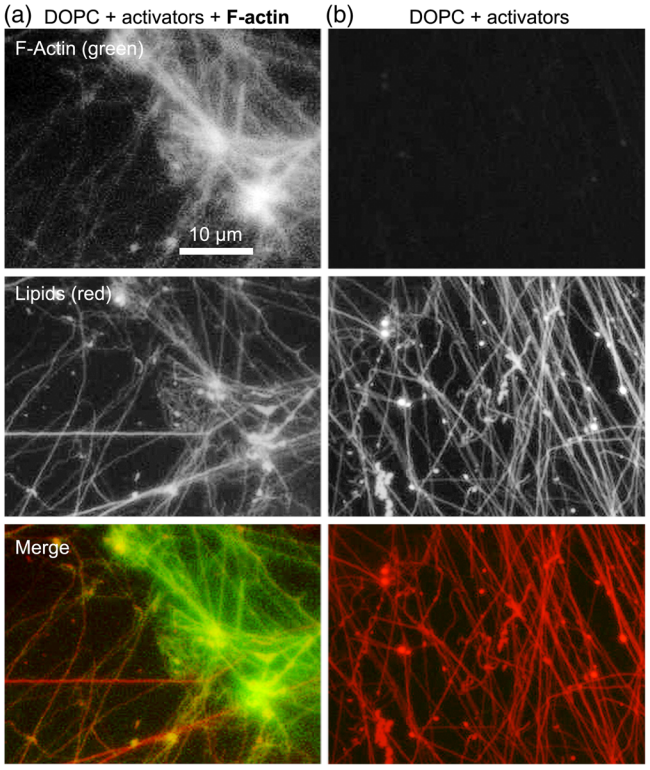

FIG. 6. Fluorescence imaging of actin filament networks on membrane nanotubes. Nanotubes are attached to a streptavidin-coated glass surface prior to incubation with actin and/or the activators of actin polymerization (essentially, SpVCA and Arp2/3; see Sec. VI for details). (a) DOPC nanotubes incubated with actin and with the activators of actin polymerization. (b) DOPC nanotubes incubated only with the activators of actin polymerization.

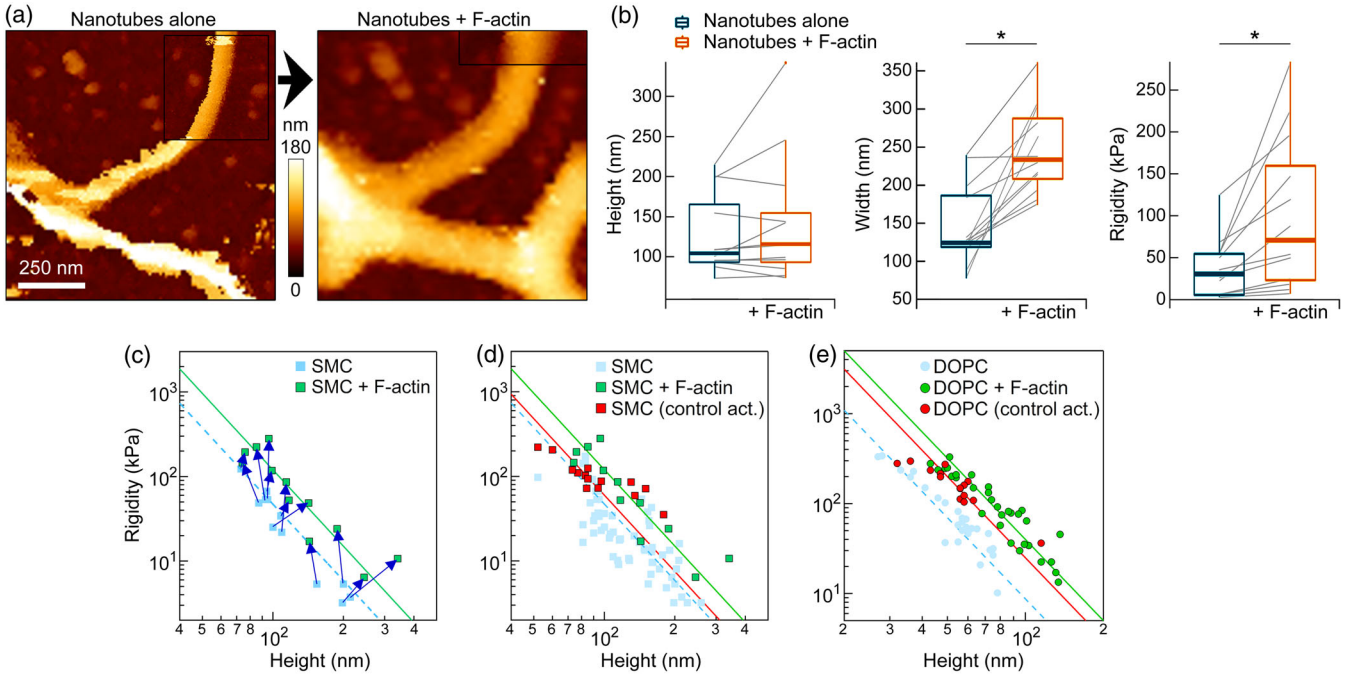

FIG. 7. Morphology and mechanics of nanotubes modified by actin. (a) AFM images of SMC nanotubes before (left) and after modification by actin and the activators of actin polymerization (right). Black rectangles delimit regions of the images scanned with a higher resolution. (b) From left to right: Heights, widths, and rigidities of the same SMC nanotubes before and after modification by actin (median and interquartile range; Wilcoxon match-paired test, $*p < 0.0005$). Heights and widths were obtained from 0 and 2 pN height maps, respectively. (c) Rigidity versus height for the same SMC nanotubes, before and after modification by actin. The solid lines represent fits to the data of the relationship $K = \chi h^{-3}$ with χ an adjustable parameter. The dashed lines are given by Eq. (4) without any adjustable parameter. (d) Rigidity versus height for all the SMC nanotubes that we analyzed over multiple experiments, including a control dataset (control act.) in which only the activators of actin polymerization were incubated with the nanotubes (but not actin). (e) Rigidity versus height for all the DOPC nanotubes that we analyzed.

with an average increase of 100 nm (an approximately twofold increase) [Fig. 7(b)]. This increase is, however, very variable, ranging from 1 to 229 nm, reflecting the heterogeneity of actin polymerization on nanotubes also observed in the fluorescence images of Fig. 6(a), and on previously studied giant vesicles [39]. This sizable increase in the nanotube width cannot be explained simply by tip convolution effects (see Sec. VI) or by the binding of SpVCA and Arp2/3. Indeed, these proteins have a combined molecular weight of 278 kDa, which corresponds to a hydrodynamic diameter of ∼12 nm [40]. Assuming an additional extension of 13 nm due to the contour length of the PEG-biotin linker [41], we deduce that SpVCA and Arp2/3 binding can at most account for an increase of the width by ∼25 nm on each side of the nanotube. Hence, in 10 out of 12 nanotubes, actin polymerization enlarges the nanotube width.

In contrast to the widths, nanotube heights are generally not changed after actin polymerization, except in the three cases where they increase by 42, 47, and 127 nm [Fig. 7(b), left-hand graph, and Fig. 7(c)]. However, even when AFM heights remain unchanged, force-extension curves collected on modified nanotubes show multiple force peaks (Fig. 8). This indicates that, as the tip retracts, it pulls some actin filaments out of the upper surface of the nanotubes. Our results suggest that filamentous actin (F-actin) forms thick networks on the sides of nanotubes, as well as flatter structures at their upper surface. Alternatively, the actin coating might change the geometry of nanotubes by flattening them. In this case, coating of the top of the tube would not cause an increase of tube height, but an even larger increase in width. However, this hypothesis is not supported by rigidity maps of actin-coated nanotubes, which clearly show that nanotubes and siding cortex form distinct regions (Fig. 9). Therefore, understanding why actin cortex accumulates more on the sides than on the top of nanotubes remains to be determined.

Actin coats increase nanotube rigidity.—Actin rigidifies the nanotubes by a factor of 3.1 ± 1.2 [Figs. 7(b)–7(d)] quite consistently across the 12 different SMC nanotubes despite their very diverse initial rigidities ($K_{\mathrm{ini}} = 2$–120 kPa). A similar increase is observed in actin-coated DOPC nanotubes [Fig. 7(e)]. We next perform control experiments where activators are present but not actin. While these activators alone do not result in a clear rigidification of the stiff SMC nanotubes [Fig. 7(d)], they induce a clear K increase in soft DOPC nanotubes compared to bare nanotubes with the same height [Fig. 7(e)]. Using Eq. (5a), we calculate the bending

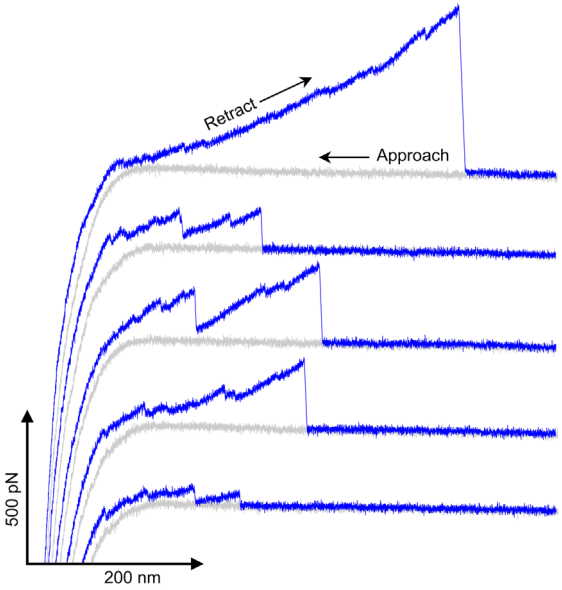

FIG. 8. Force-extension curves indicating the pulling of actin filaments from a SMC nanotube. This graph displays five distinct approach-retract cycles of the AFM tip. The retract curves clearly show some force peaks, indicating that the AFM tip pulls actin filaments or actin filament networks out of the nanotube surface when moving upward. The sudden drops in force in the retract curves indicate when the actin filaments or actin filament networks either unfold or detach from the AFM tip.

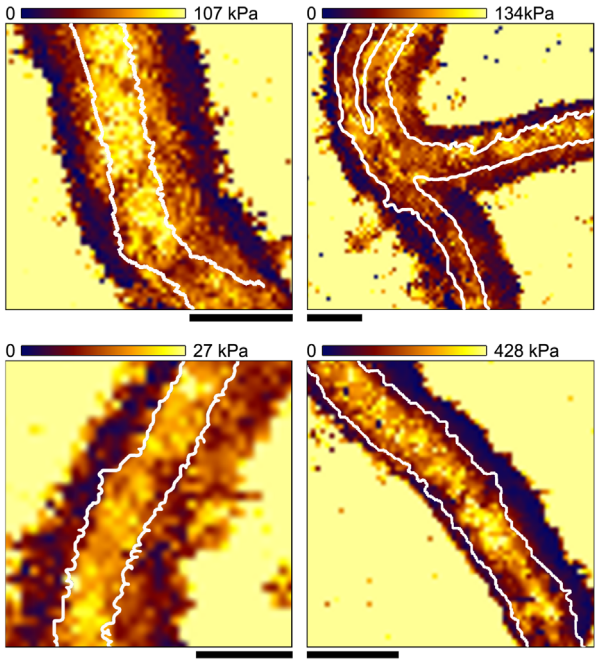

FIG. 9. AFM rigidity maps of actin-coated SMC nanotubes. In all images the white lines delimit the contours (determined from 2 pN AFM height maps; see Sec. VI) of the same nanotubes imaged prior to actin polymerization. In the four examples provided here, the actin coating clearly increases nanotube apparent width, and the actin networks siding nanotubes look softer than the nanotubes themselves.

rigidity κ of the modified nanotubes. κ is systematically higher in coated nanotubes. For SMC, κ goes from 54 ± 12 (bare tubes) to 98 ± 47 (activators present) to $131 \pm 60 k_B T$ (actin coated). We observe the same trend for DOPC, for which κ goes from 23 ± 5 to 42 ± 12 to $59 \pm 17 k_B T$ for bare, activators-coated, and actin-coated nanotubes, respectively. Consistent with the K increase, actin coats also increase the tension σ, as measured on SMC nanotubes analyzed both before ($\sigma = 0.041 \pm 0.028$) and after the coating ($\sigma = 0.080 \pm 0.055$ mN/m). This demonstrates that AFM can probe the local mechanics of protein-coated nanotubes, as well as discriminate between the roles of different proteins. This clearly sets the stage for future investigations where nanotube reshaping by diverse proteins can be characterized mechanically with high spatial resolution.

V. CONCLUSIONS

We demonstrate a simple protocol to characterize membrane nanotubes not only with AFM-like resolution and throughput, but also with pipette and optical tweezerslike mechanical accuracy. While each of these had previously been realized in separate and incompatible experimental settings, combining the best of both worlds had not been previously achieved. The strength of our protocol does not reside in its complexity or raw technical difficulty, but rather on combining a well-designed preparation and imaging protocol with an advanced understanding of the physics of the attached membrane. Both advances are easily transferable for use in other groups working on a wide range of membrane-related problems, including membranes interacting with pathological agents [42], nanomechanically tailored membranes for controlled drug delivery [16], or even biomimetic membranes that are not made of lipid bilayers [43].

From a theoretical standpoint, our fundamental insight is to design a measure of the membrane's mechanics that is unaffected by the conditions of its attachment to the substrate (adhesion energy, concentration of linking points, and critical rupture force). In that sense, our theory is universal, and the direct relationship between the rigidity of the nanotube and its height is a symptom of this universality. Furthermore, we characterize the role of local membrane fluctuations in the nanomechanics of nanotubes through the rounding of our force-displacement relation. This finding contrasts with the models usually employed to characterize the mechanics of nanotubes in standard micropipette experiments, whose large size renders fluctuations irrelevant. Finally, we show that compressed nanotubes can be highly resilient and sustain extreme lateral compression [up to 400 pN, see Fig. 3(c)] without rupturing.

We note that previous studies have used AFM to characterize membranes, although they used spherical vesicles instead of nanotubes. Vesicles have a different geometry. In vesicles the liquid is confined in a constant volume. On small unilamellar vesicles, the elastic parameters

of the membrane were calculated at low deformation by assuming that the vesicle is a spherical elastic thin shell [24]. Therefore, the tension is not considered, whereas it dominates the response of our nanotubes. Giant liposomes were also investigated [26]. Although in this case membrane tension is considered, assumptions include negligible bending stiffness and constant volume, again differing from our study.

While similar geometries have been previously used to image the assembly of biologically active proteins associated to membrane nanotubes [28], we show that our assay can be used to collect information not only on the localization but also on the mechanics of these processes. As a proof of principle, we coat the surface of the nanotube with the protein actin, which remodels the cell membrane *in vivo*, and probe its local mechanics. We detect clear changes in the morphology and mechanics of the nanotube as a result, which opens the door for characterizing the function of membrane-associated proteins with a much greater spatial resolution and throughput than is possible with current techniques. Note that previous studies using AFM force mapping have shown nanometer resolution imaging of membranes and membrane proteins [44,45]. However, in these studies the membrane is supported on a stiff surface such as mica. Here the membrane interacting with the AFM tip belongs to the top of the nanotube and undergoes thermal fluctuations as a result.

Whereas pipette methods use freestanding nanotubes, ours are attached to the surface. While this constrains the nanotube-protein geometries that can be probed by our method, this also provides an opportunity to modulate the interaction between the membrane and the surface, which changes the nanotube height and in turn gives access to different values of the membrane tension and local curvature. These are important parameters for membrane-deforming proteins [46]. For instance, as we push on the nanotube repeatedly at the same location (Fig. 2), we drive the nanotube to change its adhesion onto the substrate, as reflected by the changes in nanotube height each time the AFM tip encounters the membrane. As a result, we are in fact capable of observing the effect of multiple values of the membrane tension on a single nanotube. We thus believe that the resolution, throughput, and flexibility of our assay confer it with a great potential in addressing many biological problems involving membrane remodeling by proteins.

VI. METHODS

A. Surface preparation

Glass surfaces (35-mm-diameter FluoroDish™, with cover glass bottom, from World Precision Instruments, Sarasota, FL) are cleaned using ethanol, activated by ozone treatment, and then silanized by chemisorption of 3-aminopropyl-triethoxysilane (APTES, 97% purity, from ABCR, Karlsruhe, Germany). Formation of APTES monolayer on glass is achieved by immersing the glass in a solution of 94% methanol, 4% deionized water, 2% APTES [(v:v) "v" is volume] and 1 mM acetic acid, as described previously [47]. After 48 h the modified glass surfaces are rinsed thoroughly with ethanol, dried with a nitrogen stream, and stored in a dry environment until further use. To make a streptavidin monolayer silanized glass is immersed for 20 min in glutaraldehyde solution (12.5% in water), rinsed 3 times in water, and then immersed for 50 min in a solution of streptavidin (from Sigma-Aldrich) diluted at 5 μg/mL in Phosphate-buffered saline, a buffer solution [48]. Glutaraldehyde covalently bridges streptavidin and APTES monolayer via a chemical reaction occurring between the aldehyde and the amine groups. Modified surfaces are then rinsed using deionized water and SDS at low concentration [(0.01% w:w in water) "w" is weight] to elute noncovalently bound streptavidin. Finally, surfaces are rinsed again with water to remove salts and quickly dried with a nitrogen stream. For experiments in which actin is polymerized on nanotubes, we use glass bottom dishes: these are 35-mm-diameter petri dishes with a 10-mm-diameter glass well at their center (MatTek Corporation, Ashland, MA). Glass modification protocol of MatTek dishes is identical to that of FluoroDishes.

B. Preparation of nanotubes

1,2-dioleoyl-sn-glycero-3-phosphocholine (DOPC), N-(dodecanoyl)-sphing-4-enine-1-phosphocholine (sphingomyelin), cholesterol from ovine wool, and DSPE-PEG (2000)-biotin(1,2-distearoyl-sn-glycero-3-phosphoethanolamine-N-[biotinyl(polyethylene glycol) 2000]) (PEG-biotin lipids) are obtained from Avanti® Polar Lipids, Inc. (Alabaster, AL). Fluorescent lipids are Texas Red™ r-1,2-dihexadecanoylsn-glycero-3-phosphoethanolamine triethylammonium salt (Texas-Red™ DHPE, from ThermoFisher, Waltham, MA). DOPC, or "SMC", i.e., sphingomyelin-cholesterol mixture (at 1∶1 mol∶mol), are mixed with fluorescent lipids at 0.5% (mol:mol), and with biotinylated lipids at 1%–3% (mol:mol) and stored in chloroform at −20°C until further use. Small droplets of lipid solutions (∼0.1 μL) are deposited on the glass modified by a streptavidin monolayer. At this point, the concentration of lipids in chloroform is of ∼1.4 mg/mL, which corresponds roughly to a mass of 0.14 μg of lipids per droplet. Droplets quickly dry in ambient air; further drying using N_2 stream is performed to remove remaining traces of chloroform. Lipids are rehydrated for 1 h using *Buffer A*: 100 mM NaCl and 20 mM [(4-(2-hydroxyethyl)-1-piperazineethanesulfonic acid) HEPES] at *p*H 7.4. Then, hydrodynamic flow is generated inside the dishes using a 1 mL pipette in order to form the nanotubes. The biotin linked to lipid polar heads via PEG chain can form a very strong, specific bond with a streptavidin molecule. As a result, nanotubes attach to the surface. The solution is rinsed several times with Buffer A in order to remove lipids that are not attached to the streptavidin monolayer. In our experiments the

surface-attached nanotubes are always connected to the initial lipid reservoir, which we assume to be infinite and therefore imposing fixed tension.

C. Atomic force microscopy

Nanotubes are imaged using a Nanowizard® 4 Bioscience AFM from JPK/Bruker. Quantitative Imaging™ (QI) mode is used. In QI mode, the AFM tip is driven vertically for each pixel of the image and thus collects a force-distance curve at each approach-retract cycle. Typically, images have from 100×100 to 256×256 pixels^2 collected over surfaces of 0.4×0.4 to 4.0×4.0 μm^2. Ramp size (along the z direction) is in the range of 50–150 nm, depending on nanotube height. The vertical tip speed is set at 12–25 μm/sec, and the force setpoint (at which the tip stops its downward vertical motion and proceeds to move upward) is fixed at 50–110 pN. We use BL-AC40TS-C2 cantilevers (from Olympus) that have resonant frequency of ~25 kHz in liquid. The tip apex is in silicon and has a radius of ~8 nm. The tip-membrane interaction does not involve significant adhesion forces because the membrane does not remain in contact as the tip retracts from its surface (see Fig. 3). In all experiments the sensitivity and spring constant of the cantilever are calibrated using the noncontact thermal noise "Sader" method [49], which preserves the tip apex from undergoing any damage before probing samples. In our experiments the spring constant is always in a range of 0.09–0.12 N/m, close to the nominal value of 0.09 N/m provided by the manufacturer. However, uncertainties related to the exact lateral size of the cantilever and hydrodynamic damping in liquid are always present, and thus we estimate that this calibration method induces an error of up to 30% on the spring constant. In all AFM images the background surface is flattened after processing the force-displacement curves (see next paragraph). In some images a median filter is used to replace obvious outlier pixel values (in height or rigidity maps) with the median value of neighboring pixels, without affecting the overall distribution of heights and rigidities.

D. Analysis of force-displacement curves

Force curves are processed using the JPK Data Processing software (version 6.1). In all force curves the piezoheight is corrected with the deflection of the cantilever in order to get the accurate vertical tip position, which is then plotted as a function of the force. To determine the rigidity K and the contact point height, we use a simple model that describes the parabolic relationship between the indentation depth δ and the force f that deforms the membrane: $f = K\delta^2$. To determine the rigidity of one nanotube (as in Fig. 5), we fit this model to all the force-displacement curves that are collected over the nanotube. Because the contact geometry at the nanotube borders is unclear, we select a region of interest (ROI) that always corresponds to the central regions of the nanotubes (see Fig. 10). The rigidity of the nanotube is the result of averaging all the rigidities determined for each individual force curve that belong to the ROI. The number of force curves collected for one nanotube varies according to the nanotube size and to the resolution in each AFM image; it is on the order of at least a hundred (and up to tens of

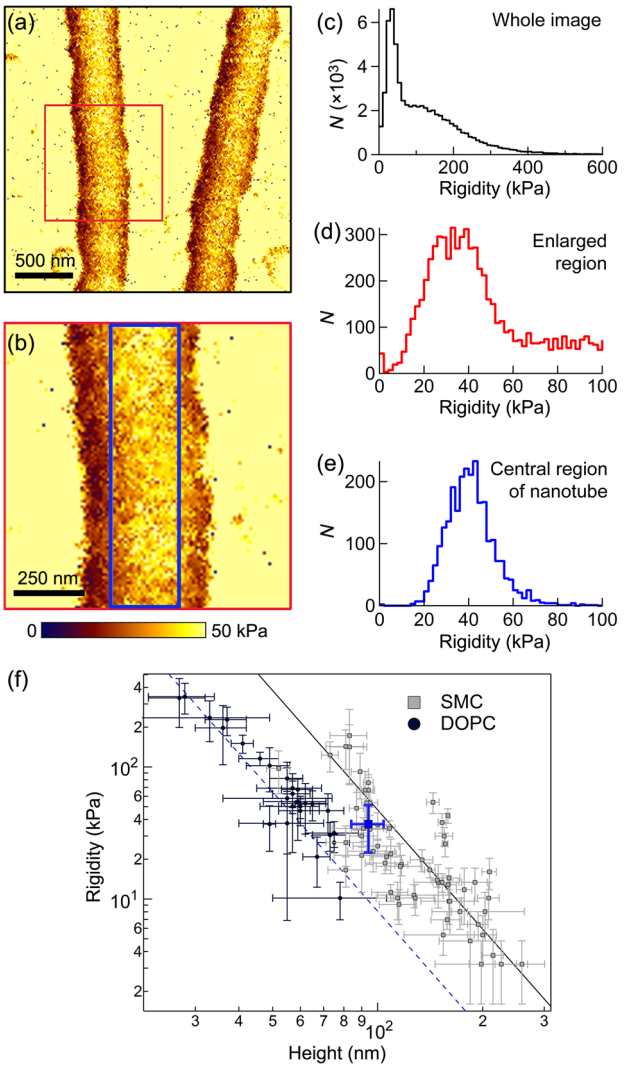

FIG. 10. Measuring the rigidity of a nanotube. (a) AFM rigidity map of two nanotubes. Red square: region enlarged in (b). (b) Enlarged region of the AFM map in (a). (c)–(e) Distributions of the rigidity K in the AFM images. (c) Distribution of K in the entire image in (a). Blue rectangle: central region of the nanotube. (d) Distribution of K in the red square in (a), i.e., in the entire image in (b). (e) Distribution of K in the region delimited by a blue rectangle in (b). A Gaussian is fitted to the data to determine the K (mean plus or minus 1 s.d.) of the nanotube. Here the Gaussian fit results in $K = 38 \pm 14$ kPa. (f) Rigidity versus height for all bare nanotubes. The data points are the same as in Fig. 5; in addition, here we display the error bars on the height and rigidity. The data point in blue corresponds to the nanotube analyzed in (b) and (e).

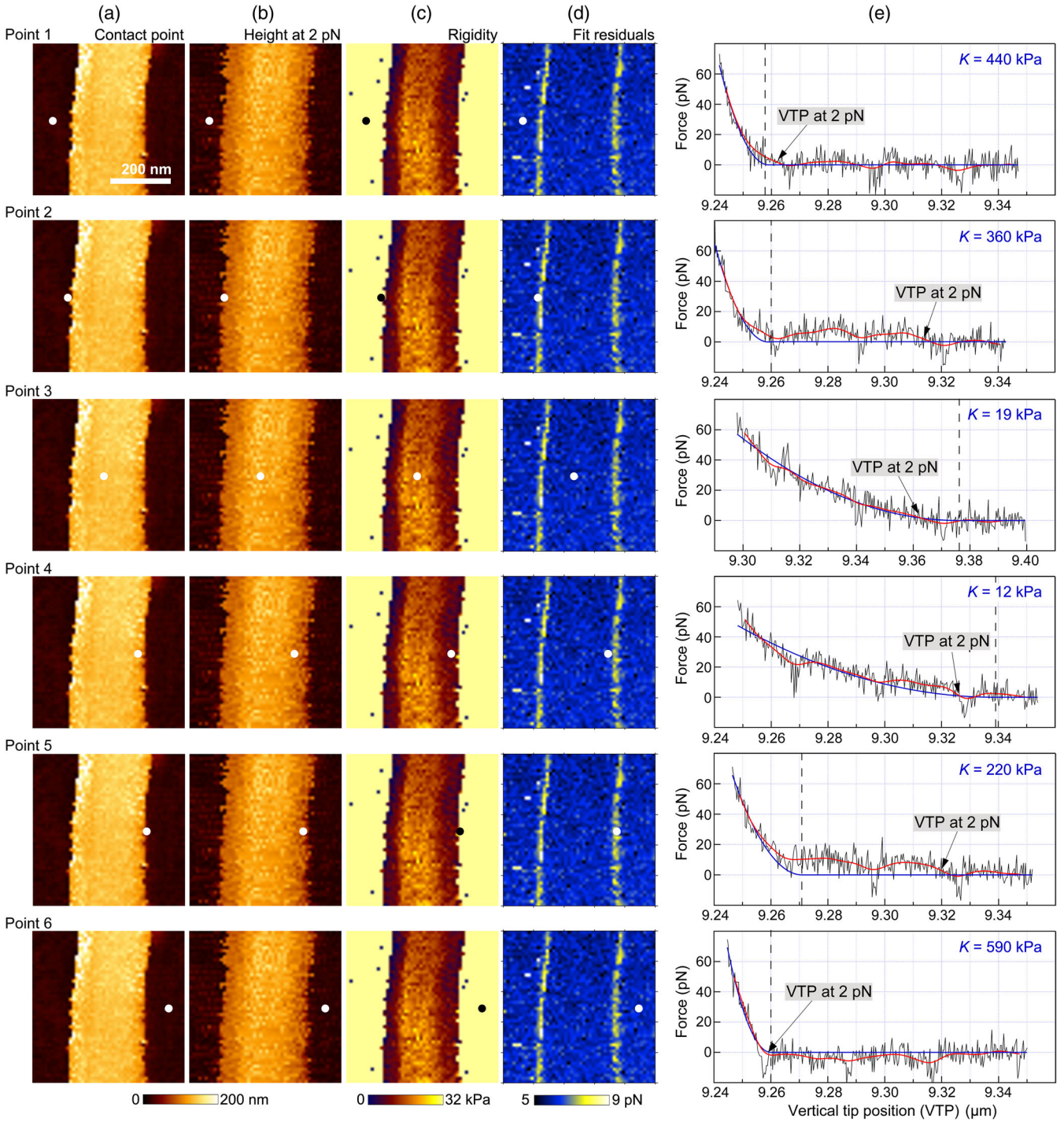

FIG. 11. Determination of the height and width of a membrane nanotube. (a) Contact point (i.e., height at zero force) maps. (b) Maps of the height at 2 pN. (c) Rigidity maps. (d) Maps of fit residuals. (e) Force-distance curves collected at locations marked by dots in the maps of (a)–(d). The red lines are the results of smoothing the force curves and are used to build the 2 pN height maps, which provide the best description of the nanotube width. The blue lines come from least-squares fitting of the data using $f = K\delta^2$ for $\delta > 0$, where f is the force, K the rigidity, and δ the indentation depth. Vertical dashed lines show the position where $\delta = 0$ that we use to determine the local nanotube height. Note that, at points 2 and 5 (edges of the nanotube), the force starts increasing but quickly drops, which indicates that the nanotube has been pushed laterally by the AFM tip. As a result, the contact point and 2 pN height maps show clear differences.

thousands). The zero-force height, which is equivalent to the "contact point" height, is extrapolated from fitting the equation above to the force-displacement curves [see Figs. 2(b) and 3]. AFM height maps at higher forces, i.e., at 2 and 50 pN, are obtained differently. Instead of fitting a model to the force curve, the force curve is filtered by using a smoothing function and the height at the chosen force (2 or 50 pN) is picked from the smoothed curve; i.e., it corresponds to the first time at which the smoothed curve crosses the 2 or 50 pN line, starting from the maximum force. Hence, using the height mapping at a force of 2 pN, it is possible to visualize small tip height variations that are otherwise buried in the thermal noise (at least ∼10 pN in AFM experiments). Such small variations are detected at the edges of nanotubes (see Fig. 11). In fact, carefully inspecting the force curves collected at the nanotube edges reveals that, as the AFM tip (moving vertically downward) encounters the nanotube, the force increases a bit, after which it suddenly drops because the tip pushes the nanotube sideways. Then, the force rises again as the tip reaches the underlying stiff substrate. As a result, the nanotube edges disappear from the AFM height maps obtained at zero force and at 50 pN, but not necessarily from the 2 pN AFM height maps. We conclude that using the 2-pN-force AFM height maps it is possible to derive better estimations of the nanotube widths than when using the zero-force and 50-pN-force AFM height maps.

E. Morphology of nanotubes

The heights and widths of nanotubes are inferred from zero-force and 2 pN height maps, respectively. The same ROI that is selected to calculate the rigidity of a given nanotube (see above) is also used to calculate its height. All individual heights within the ROI are averaged and the calculated mean is the height of the nanotube. Width is measured by tracing a straight line that goes from one nanotube side to the other (perpendicular to the longitudinal axis). At least 15 nanotube sections are measured to collect width at different locations along the nanotube, and the width of a nanotube is the mean of all these measurements. The heights and widths are then used to calculate their aspect ratios and cross-sectional areas. However, prior to this, suitable nanotubes must be selected. In fact, some nanotubes display high levels of heterogeneity and must be discarded from the analysis. For instance, if the width of a given nanotube varies a lot (to the point where it sometimes appears to be cut), then we cannot use it. In this case, the nanotube has apparently disassembled, and what remained of it is a lipid bilayer that spread over the streptavidin monolayer. Therefore, only nanotubes that appear to have rather homogeneous widths (and well-defined borders) are selected for measurements of nanotube height and width. The aspect ratio corresponds to the width divided by the height. Hence, aspect ratios of ∼1 or $\gg 1$ indicate cylindrical or flattened nanotubes, respectively. We tested the potential dependence of aspect ratio on the concentration of biotinylated lipids contained in the lipid mixture and found no correlation for concentrations of 1%–3% (mol:mol). Cross-sectional areas C are calculated assuming an ellipsoid shape for the nanotube section, using height h and width w as parameters to determine $C = \pi hw/4$. In one experiment we measured the sizes of the same nanotubes before and after modification by actin. Note that in this experiment, tip convolution effects could be neglected because (i) we changed the AFM tip right before imaging the modified nanotubes and (ii) there is one occurrence of a nanotube whose width did not increase after the actin treatment (+1 nm only). If the tip had picked up some material during scanning, even this nanotube would have displayed an increased width.

F. Actin polymerization

A solution of 30 $\mu\text{mol} \cdot \text{L}^{-1}$ monomeric actin (Cytoskeleton, Denver, CO) containing 15% of labeled actin-488 (Molecular Probes, Eugene, OR) is obtained by incubating the actin solution in G-Buffer (2 mM tris at pH 8.0, 0.2 mM $CaCl_2$, 0.2 mM Dithiothreitol, and 0.2 mM adenosine triphosphate) over 2 days at 4°C. The activator of polymerization SpVCA is purified as described in Ref. [50]. After formation of nanotubes in the MatTek dish, SpVCA is incubated for 15 min to a final concentration of ∼300 $\text{nmol} \cdot \text{L}^{-1}$ in ∼100 μL of solution. Then, polymerization buffer (1 mM tris at pH 7.4, 50 mM KCl, 2 mM $MgCl_2$, 0.1 mM DTT, 2 mM ATP, 0.02 g/L β-casein and 95 mM sucrose; osmolarity, 200 mOsm/kg) is added to dilute the unbound SpVCA until its concentration has decreased below 3 $\text{nmol} \cdot \text{L}^{-1}$, which is low enough to avoid bulk polymerization. Next, actin polymerization on nanotubes is initiated by adding a solution of 37 $\text{nmol} \cdot \text{L}^{-1}$ porcine Arp2/3 (Cytoskeleton, Denver, CO), 25 $\text{nmol} \cdot \text{L}^{-1}$ mouse $\alpha 1\beta 2$ capping protein (purified as in Ref. [51]), 3 $\mu\text{mol} \cdot \text{L}^{-1}$ of the monomeric actin solution, and 3 $\mu\text{mol} \cdot \text{L}^{-1}$ profilin (purified as in Ref. [50]). Actin is left to polymerize in the chamber for 20–30 min. Finally, the polymerization reaction is quenched by adding 2 mL of Buffer A. In a first control experiment we test the effects of the activators of actin polymerization by using the exact same protocol except that actin is removed from the last solution [see Fig. 6]. In a second control experiment we incubate nanotubes with an actin solution but without the activators of polymerization, and we do not observe any green fluorescence (which signals the presence of F-actin).

ACKNOWLEDGMENTS

We thank Cécile Sykes for providing help with the actin experiments and for reading and commenting our manuscript. We also thank Luca Barberi for useful discussions about modeling our AFM measurements. We acknowledge funding from the Université of Evry-Paris Saclay, from the

CNRS, from the Genopole Biocluster at Evry (Research associate fellowship to G. L.), and from the French Agence Nationale de la Recherche (ANR-18-CE13-0007-01 awarded to C. C.). M. L. is supported by ANR Grant No. ANR-15-CE13-0004-03 and ERC Starting Grant No. 677532. Our group belongs to the CNRS consortium CellTiss. This work was supported by the Paris Ile-de-France Region/Respore program.

APPENDIX A: THEORETICAL DERIVATION OF THE FORCE-DISPLACEMENT RELATION

Here we derive the theoretical arguments leading to the relations presented in Sec. III between the membrane mechanical parameters (bending rigidity κ and tension σ) and the thickness h and rigidity K of the membrane nanotubes. Our calculations consider a finite-size (i.e., not pointlike) indenter.

Depending on the strength of the interactions between the adherent surface and the lipids, the nanotube may be cylindrical or flattened, as illustrated in Fig. 12. Here, we first ignore thermal fluctuations and consider two limiting cases. In Appendix A1 we consider the narrow, cylindrical nanotube illustrated in Fig. 12(a). In Appendix A2 we discuss the opposite limit of the wide, substantially flattened nanotube of Fig. 12(b). Finally, we show in Appendix A3 that while these calculations do not account for the experimentally observed rounding of the force-displacement curves, thermal fluctuations do, which enables our analysis of the AFM data.

Our approach is designed to bypass two prohibitively difficult nanotube rigidity calculations. First, we do not explicitly model partially flattened nanotubes ($w \gg h$ in the notation of Fig. 12). This is indeed unnecessary since the narrow and wide cases studied in Appendixes A1 and A2 both result in the same rigidity scaling, implying that this scaling can be extended to intermediate, partially flattened nanotubes. Second, in Appendix A3 we incorporate thermal fluctuations without describing the membrane's full conformational fluctuations, but through a single effective degree of freedom. Despite these simplifications, Fig. 6 shows that our approach accurately predicts the experimental dependence of K on the nanotube height and on the membrane bending modulus, which validates the cornerstone of our approach.

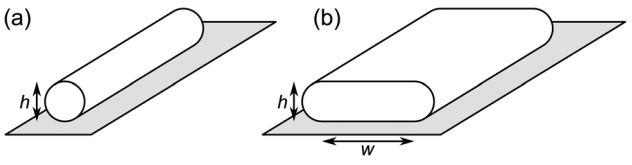

FIG. 12. Nanotube morphologies considered here. (a) When the adhesion between the (white) lipids and the (gray) adherent surface is very weak, the membrane shape is determined by the balance between its bending rigidity and its tension, resulting in a cylindrical morphology. (b) In the opposite limit of strong adhesion, the nanotube undergoes significant flattening ($w \gg h$).

1. Dimensional argument for a narrow nanotube

We consider a nanotube composed of a thin membrane with bending modulus κ connected to a membrane reservoir imposing its tension σ. In the absence of thermal fluctuations, the shape of the nanotube thus minimizes the Helfrich free energy [52],

$$\mathscr{H} = \iint \left(\frac{\kappa}{2}c^2 + \sigma\right) dS, \tag{A1}$$

where c is the local total curvature of the membrane and where the integral runs over its surface. In our description the binding of the nanotube to the adherent surface is enforced through a boundary condition at the location where the membrane touches the surface. Qualitatively, a weak binding will impose a small contact area between the membrane and the surface as in Fig. 12(a), while a strong binding leads to the morphology of Fig. 12(b). In the former case, the nanotube is simply a cylinder with diameter h and length L and Eq. (A1) reduces to

$$\mathscr{H} = \left(\frac{2\kappa}{h^2} + \sigma\right) \pi h L, \tag{A2}$$

which we minimize over h to find

$$h = \sqrt{\frac{2\kappa}{\sigma}}. \tag{A3}$$

When indented from the top as in an AFM experiment, the nanotube responds as a Hookean spring with constant k. As κ and σ are the only parameters involved, from a dimensional standpoint the spring constant must scale as

$$k \approx \sigma \approx \frac{\kappa}{h^2}. \tag{A4}$$

This scaling form is valid both for a pointlike and a locally flat indenter, implying that it holds irrespective of the detailed shape of the indenter. Note that as further discussed in Appendix A3, k is not identical to the measured nanotube rigidity K, even though they are closely related.

2. Full calculation for a wide nanotube

The simple reasoning leading to Eq. (A4) does not apply to the wide nanotube of Fig. 12(b) due to the presence of two additional length scales, namely, the width w of the nanotube and the radius R of the indenter tip. Here we compute the spring constant k as a function of the bending modulus κ and surface tension σ in this more complex situation.

While the bending modulus is intrinsic to the membrane, the surface tension is much less controlled in our experiments. It can, however, be inferred from the nanotube height: indeed, in the geometry of Fig. 12(b), the sides of the nanotube are well approximated by two half cylinders at mechanical equilibrium under the effect of their tension and bending modulus. This situation is very similar to that leading to Eq. (A3), implying the same relationship between cylindrical diameter and membrane tension:

$$\sigma \approx \frac{2\kappa}{h^2}. \tag{A5}$$

Taking advantage of this readout for the tension, here we compute the deformation of the membrane when the indenter is lowered over a distance δ [Fig. 13(a)]. While the top face of a real nanotube is a rectangular membrane patch of width w, in our calculation we approximate it to a circular patch of diameter w. This simplification hardly changes our result, as the outer boundary condition only intervenes there as a (weak) logarithmic correction, as shown below. In Appendix A2a, we derive the mechanical equilibrium equations for this problem. We next solve them in Appendix A2b and derive a closed-form expression for the spring constant k.

a. Mechanical equilibrium equations

We describe the deformation of our membrane disk by a vertical displacement field $u(r)$, with r the radial coordinate. We use the position of the indenter tip as our altitude reference, implying that in our reference frame the indenter tip is fixed while the rim of the membrane is raised by δ:

$$u(0) = 0 \quad \text{and} \quad u(w/2) = \delta. \tag{A6}$$

We denote by R the radius of curvature of the indenter tip and by x the radius of the indenter-membrane contact. For small x, we can approximate the shape of the indenter by a parabola, implying two additional boundary conditions:

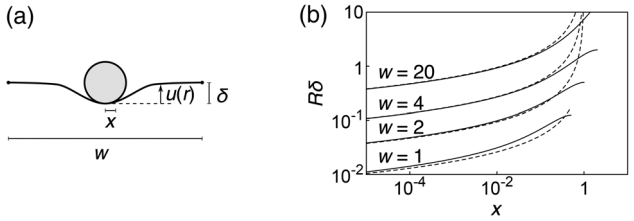

FIG. 13. Wide nanotube deformation. (a) Parametrization of the membrane deformation induced by the (gray) indenter. (b) Nonlinear relation between the indentation depth δ and the contact radius x depending on the dimensionless membrane width w. Solid lines represent the full relation of Eq. (A14), and dashed lines picture the $\delta \to 0$ asymptotic relation of Eq. (A15).

$$u(x) = \frac{x^2}{2R} \quad \text{and} \quad u'(x) = \frac{x}{R}. \tag{A7}$$

The latter condition derives from the existence of the membrane bending modulus, which forbids discontinuities in the membrane's slope. This condition has interesting implications for cases where the indentation is produced by a conical, not spherical, indenter. In such a situation, the continuity of the membrane's slope forces it to remain horizontal at the tip of the indenter, implying the indenter acts as if it were pointlike. Therefore, here the conical contact law can be recovered as the $R \to 0$ limit of the spherical one, which contrasts with the classical Hertz-Sneddon models for the indentation of an elastic medium in the absence of a bending modulus.

For small deformations u, we can rewrite the free energy of Eq. (A1) in the Monge gauge as

$$\mathcal{H} = \int \left(\frac{(\Delta u)^2}{2} + \frac{(\nabla u)^2}{2} \right) 2\pi r dr, \tag{A8}$$

where we use a set of dimensionless units where $\kappa = 1$ and $\sigma = 1$. Noting that $u(r) = r^2/2R$ for $r \leq x$ and minimizing $\mathcal{H}$ over x as well as the displacement $u(r)$ for $r \in [x, w/2]$ yields two more boundary conditions,

$$\Delta u(x) = \frac{2}{R} \quad \text{and} \quad \Delta u\left(\frac{w}{2}\right) = 0, \tag{A9}$$

and a bulk equation,

$$\Delta^2 u = \Delta u, \tag{A10}$$

valid in the freestanding membrane domain $r \in [x, w/2]$.

To compute the force required to maintain the indenter's altitude, we remove the constraint $u(w/2) = 0$ and instead add a term $-fu(L)$ to $\mathcal{H}$. Minimizing over u under these conditions yields

$$f = -\pi w[\partial_r(\Delta u - u)](r = w/2), \tag{A11}$$

implying that the indenter force can be directly computed from the displacement field of the membrane.

b. Effective spring constant

Integrating Eq. (A10) yields

$$u(r) = aI_0(r) + bK_0(r) + c \ln r + d, \tag{A12}$$

where a, b, c, and d are integration constants and I_0 and K_0 are the modified Bessel functions of the first and second kind, respectively [35]. Combining this expression with Eqs. (A6), (A7), and (A9) yields

$$u(r) = \frac{2}{R}\frac{K_0(w/2)I_0(r) - I_0(w/2)K_0(r)}{K_0(w/2)I_0(x) - I_0(w/2)K_0(x)} - \left(\frac{4-x^2}{2R} + \delta\right)\frac{\ln(2r/w)}{\ln(2x/w)} + \delta, \tag{A13}$$

where the contact radius x is given as the solution of

$$R\delta = \frac{x^2}{2} - 2 + 2x\ \ln\frac{2x}{w}\left[\frac{K_0(w/2)I_1(x) + I_0(w/2)K_1(x)}{K_0(w/2)I_0(x) - I_0(w/2)K_0(x)} - \frac{x}{2}\right]. \tag{A14}$$

Note that the right-hand side of Eq. (A14) vanishes at $x = 0$, then increases monotonically with x all the way up to $x = w/2$, as shown in Fig. 13(b). This implies that Eq. (A14) always has a unique solution for small indentations δ, and that $x \underset{\delta\to 0}{\longrightarrow} 0$. For weak indentations, Eq. (A14) thus simplifies to

$$R\delta = \frac{\alpha(w)}{\ln(1/x)}, \quad \text{with} \quad \alpha(w) = 2\left(\gamma + \ln\frac{w}{4} + \frac{K_0(w/2)}{I_0(w/2)}\right), \tag{A15}$$

which we also plot in Fig. 13(b) and where $\gamma \simeq 0.577\,216$ is the Euler gamma constant. Inverting this equation, plugging back into Eq. (A13), and using Eq. (A11) finally yields

$$f = \begin{cases} 0 & \text{if } \delta < 0 \\ k\delta & \text{if } \delta \geq 0, \end{cases} \tag{A16}$$

with $k = 4\pi\delta/\alpha(w)$, implying the following expression in dimensional units:

$$k = \frac{4\pi\sigma}{\alpha(w\sqrt{\sigma/\kappa})} = \frac{4\pi\kappa}{h^2\alpha(\sqrt{2}w/h)}. \tag{A17}$$

Finally, as discussed in the Appendix, we consider the limit where the nanotube is much wider than tall $h \ll w$, yielding

$$k \underset{h\ll w}{\sim} \frac{2\pi}{\gamma + \ln(w/\sqrt{2}h)}\frac{\kappa}{h^2}, \tag{A18}$$

which has the same scaling in κ and h as Eq. (A4) up to a weak (for $h \ll w$) logarithmic dependence in the system size, which we treat as a constant in our fits. In conclusion, since small-w and large-w nanotubes both have a spring constant $k \approx \kappa/h^2$, this scaling should give a reasonable description of nanotubes of any width.

3. Rounding of the force-displacement relation by thermal fluctuations

The zero-temperature force-displacement relation of Eq. (A16) does not display the rounded shape apparent in Figs. 2(b) and 3 and fitted there using the quadratic fit

$$f_{\text{quad}}(\delta) = \begin{cases} 0 & \text{if } \delta < 0 \\ K\delta^2 & \text{if } \delta \geq 0. \end{cases} \tag{A19}$$

Here we reconcile these two apparently contradictory force-displacement relations and relate k and K by introducing thermal fluctuations in our theory.

We describe membrane fluctuations as a single fluctuating degree of freedom u representing the altitude of the central point of the membrane. This represents an approximation compared to the full deformation field studied in Appendix A2. The variable u is confined by a harmonic potential with rigidity k, hence a potential energy $ku^2/2$, and the presence of the indenter imposes $u < -\delta$. As a result of this constraint, the partition function of the system reads

$$Z(\delta) = \int_{-\infty}^{-\delta} e^{-ku^2/2k_BT}du, \tag{A20}$$

where k_BT is the thermal energy. The free energy of the system reads $F(\delta) = -k_BT\ \ln Z(\delta)$, implying an average restoring force on the indenter,

$$f_{\text{thermal}}(\delta) = -\frac{dF}{d\delta} = \sqrt{\frac{2kk_BT}{\pi}}\frac{e^{-k\delta^2/2k_BT}}{\text{erfc}(\delta\sqrt{k/2k_BT})}, \tag{A21}$$

where erfc is the complementary error function [35]. This expression reveals that the standard fitting form given by Eq. (A19), which was chosen because it is easily implemented using standard AFM software, is not in fact

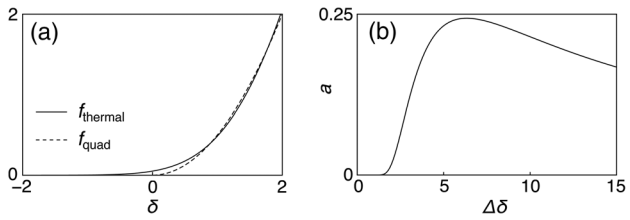

FIG. 14. Correspondence between the heuristic force dependence of Eq. (A19) and the theoretical expression of Eq. (A21). Here we use dimensionless units such that $k = 1$ and $k_BT = 1$. (a) Best fit of $f_{\text{quad}}(\delta + \delta_0)$ to $f_{\text{thermal}}(\delta)$ over the interval $\delta \in [-2, 2]$ using as fitting parameters δ_0 and the coefficient a from Eq. (A22). (b) Best-fit value obtained for a when performing the fit over an interval $\delta \in [-\Delta\delta/2, \Delta\delta/2]$ as a function of $\Delta\delta$. For our experimental data, $\Delta\delta$ is typically comprised between 3 and 5.

identical to the form of Eq. (A21) given by our theory. However, we show in Fig. 14(a) that the two expressions are in practice indistinguishable in the presence of noise and when the comparison is performed in a finite δ windows typical of our experiments. Dimensionally, the relation between the rigidities in the two descriptions must read

$$K = a\frac{k^{3/2}}{\sqrt{k_B T}}, \tag{A22}$$

where a is a numerical prefactor. As shown in Fig. 14(b), depending on the δ window used, the best fit between the two functional forms is obtained for values of a comprised between 0.1 and 0.25. Combining this result with Eq. (A18) yields the dependence discussed in the main text.

[1] K. McCoy-Simandle, S. J. Hanna, and D. Cox, *Exosomes and Nanotubes: Control of Immune Cell Communication*, Int. J. Biochem. Cell Biol. **71**, 44 (2016).

[2] A. Roux, *The Physics of Membrane Tubes: Soft Templates for Studying Cellular Membranes*, Soft Matter **9**, 6726 (2013).

[3] P. Bassereau *et al.*, *The 2018 Biomembrane Curvature and Remodeling Roadmap*, J. Phys. D **51**, 343001 (2018).

[4] L. M. Westrate, J. E. Lee, W. A. Prinz, and G. K. Voeltz, *Form Follows Function: The Importance of Endoplasmic Reticulum Shape*, Annu. Rev. Biochem. **84**, 791 (2015).

[5] M. A. De Matteis and A. Luini, *Exiting the Golgi Complex*, Nat. Rev. Mol. Cell Biol. **9**, 273 (2008).

[6] S. Morlot, V. Galli, M. Klein, N. Chiaruttini, J. Manzi, F. Humbert, L. Dinis, M. Lenz, G. Cappello, and A. Roux, *Membrane Shape at the Edge of the Dynamin Helix Sets Location and Duration of the Fission Reaction*, Cell **151**, 619 (2012).

[7] J. Schoneberg *et al.*, *ATP-Dependent Force Generation and Membrane Scission by ESCRT-III and Vps4*, Science **362**, 1423 (2018).

[8] M. Simunovic, P. Bassereau, and G. A. Voth, *Organizing Membrane-Curving Proteins: The Emerging Dynamical Picture*, Curr. Opin. Struct. Biol. **51**, 99 (2018).

[9] M. Kaksonen, C. P. Toret, and D. G. Drubin, *Harnessing Actin Dynamics for Clathrin-Mediated Endocytosis*, Nat. Rev. Mol. Cell Biol. **7**, 404 (2006).

[10] J. Lemiere, F. Valentino, C. Campillo, and C. Sykes, *How Cellular Membrane Properties Are Affected by the Actin Cytoskeleton*, Biochimie **130**, 33 (2016).

[11] S. Miserey-Lenkei, G. Chalancon, S. Bardin, E. Formstecher, B. Goud, and A. Echard, *Rab and Actomyosin-Dependent Fission of Transport Vesicles at the Golgi Complex*, Nat. Cell Biol. **12**, 645 (2010).

[12] W. Roemer *et al.*, *Actin Dynamics Drive Membrane Reorganization and Scission in Clathrin-Independent Endocytosis*, Cell **140**, 540 (2010).

[13] G. Smolyakov, B. Thiebot, C. Campillo, S. Labdi, C. Severac, J. Pelta, and E. Dague, *Elasticity, Adhesion, and Tether Extrusion on Breast Cancer Cells Provide a Signature of Their Invasive Potential*, ACS Appl. Mater. Interfaces **8**, 27426 (2016).

[14] A. Karlsson, R. Karlsson, M. Karlsson, A. S. Cans, A. Stromberg, F. Ryttsen, and O. Orwar, *Molecular Engineering: Networks of Nanotubes and Containers*, Nature (London) **409**, 150 (2001).

[15] M. Karlsson, K. Sott, M. Davidson, A. S. Cans, P. Linderholm, D. Chiu, and O. Orwar, *Formation of Geometrically Complex Lipid Nanotube-Vesicle Networks of Higher-Order Topologies*, Proc. Natl. Acad. Sci. U.S.A. **99**, 11573 (2002).

[16] T. Bhatia, J. Agudo-Canalejo, R. Dimova, and R. Lipowsky, *Membrane Nanotubes Increase the Robustness of Giant Vesicles*, ACS Nano **12**, 4478 (2018).

[17] M. Simunovic *et al.*, *Friction Mediates Scission of Tubular Membranes Scaffolded by BAR Proteins*, Cell **170**, 172 (2017).

[18] P. J. Carman and R. Dominguez, *BAR Domain Proteins—A Linkage between Cellular Membranes, Signaling Pathways, and the Actin Cytoskeleton*, J. Cell Sci. **10**, 1587 (2018).

[19] C. Leduc, O. Campas, J. F. Joanny, J. Prost, and P. Bassereau, *Mechanism of Membrane Nanotube Formation by Molecular Motors*, BBA-Biomembranes **1798**, 1418 (2010).

[20] S. Dar, S. C. Kamerkar, and T. J. Pucadyil, *A High-Throughput Platform for Real-Time Analysis of Membrane Fission Reactions Reveals Dynamin Function*, Nat. Cell Biol. **17**, 1588 (2015).

[21] K. Guevorkian, J. Manzi, L. L. Pontani, F. Brochard-Wyart, and C. Sykes, *Mechanics of Biomimetic Liposomes Encapsulating an Actin Shell*, Biophys. J. **109**, 2471 (2015).

[22] C. Prevost, F. C. Tsai, P. Bassereau, and M. Simunovic, *Pulling Membrane Nanotubes from Giant Unilamellar Vesicles*, J. Vis. Exp. **130**, e56086 (2017).

[23] F. Valentino, P. Sens, J. Lemiere, A. Allard, T. Betz, C. Campillo, and C. Sykes, *Fluctuations of a Membrane Nanotube Revealed by High-Resolution Force Measurements*, Soft Matter **12**, 9429 (2016).

[24] N. Delorme and A. Fery, *Direct Method to Study Membrane Rigidity of Small Vesicles Based on Atomic Force Microscope Force Spectroscopy*, Phys. Rev. E **74**, 030901 (2006).

[25] L. Picas, F. Rico, and S. Scheuring, *Direct Measurement of the Mechanical Properties of Lipid Phases in Supported Bilayers*, Biophys. J. **102**, L01 (2012).

[26] E. Schafer, M. Vache, T. T. Kliesch, and A. Janshoff, *Mechanical Response of Adherent Giant Liposomes to Indentation with a Conical AFM-Tip*, Soft Matter **11**, 4487 (2015).

[27] Y. Zhao, K. Tamhane, X. Zhang, L. An, and J. Fang, *Radial Elasticity of Self-Assembled Lipid Tubules*, ACS Nano **2**, 1466 (2008).

[28] A. Colom, L. Redondo-Morata, N. Chiaruttini, A. Roux, and S. Scheuring, *Dynamic Remodeling of the Dynamin Helix during Membrane Constriction*, Proc. Natl. Acad. Sci. U.S.A. **114**, 5449 (2017).

[29] R. Lipowsky, *Coupling of Bending and Stretching Deformations in Vesicle Membranes*, Adv. Colloid Interface Sci. **208**, 14 (2014).

[30] M. Bovellan *et al.*, *Cellular Control of Cortical Actin Nucleation*, Curr. Biol. **24**, 1628 (2014).

[31] N. Morone, T. Fujiwara, K. Murase, R. S. Kasai, H. Ike, S. Yuasa, J. Usukura, and A. Kusumi, *Three-Dimensional Reconstruction of the Membrane Skeleton at the Plasma Membrane Interface by Electron Tomography*, J. Cell Biol. **174**, 851 (2006).

[32] W. Rawicz, K. C. Olbrich, T. McIntosh, D. Needham, and E. Evans, *Effect of Chain Length and Unsaturation on Elasticity of Lipid Bilayers*, Biophys. J. **79**, 328 (2000).

[33] A. Roux, D. Cuvelier, P. Nassoy, J. Prost, P. Bassereau, and B. Goud, *Role of Curvature and Phase Transition in Lipid Sorting and Fission of Membrane Tubules*, EMBO J. **24**, 1537 (2005).

[34] D. R. Daniels, D. Marenduzzo, and M. S. Turner, *Stall, Spiculate, or Run Away: The Fate of Fibers Growing towards Fluctuating Membranes*, Phys. Rev. Lett. **97**, 098101 (2006).

[35] M. Abramowitz, *Handbook of Mathematical Functions, with Formulas, Graphs, and Mathematical Tables* (Dover Publications, Inc., New York, 1974).

[36] N. C. Gauthier, T. A. Masters, and M. P. Sheetz, *Mechanical Feedback between Membrane Tension and Dynamics*, Trends Cell Biol. **22**, 527 (2012).

[37] A. D. Lieber, S. Yehudai-Resheff, E. L. Barnhart, J. A. Theriot, and K. Keren, *Membrane Tension in Rapidly Moving Cells Is Determined by Cytoskeletal Forces*, Curr. Biol. **23**, 1409 (2013).

[38] C. Simon, V. Caorsi, C. Campillo, and C. Sykes, *Interplay between Membrane Tension and the Actin Cytoskeleton Determines Shape Changes*, Phys. Biol. **15**, 065004 (2018).

[39] V. Caorsi, J. Lemiere, C. Campillo, M. Bussonnier, J. Manzi, T. Betz, J. Plastino, K. Carvalho, and C. Sykes, *Cell-Sized Liposome Doublets Reveal Active Tension Build-Up Driven by Acto-Myosin Dynamics*, Soft Matter **12**, 6223 (2016).

[40] K. R. Cho, Yu Huang, S. Yu, S. Yin, M. Plomp, S. R. Qiu, R. Lakshminarayanan, J. Moradian-Oldak, M.-S. Sy, and J. J. De Yoreo, *A Multistage Pathway for Human Prion Protein Aggregation In Vitro: From Multimeric Seeds to Beta-Oligomers and Nonfibrillar Structures*, J. Am. Chem. Soc. **133**, 8586 (2011).

[41] Z. Ma, D. N. LeBard, S. M. Loverde, K. A. Sharp, M. L. Klein, D. E. Discher, and T. H. Finkel, *TCR Triggering by pMHC Ligands Tethered on Surfaces Via Poly(Ethylene Glycol) Depends on Polymer Length*, PLoS One **9**, e112292 (2014).

[42] L. Johannes and W. Romer, *Shiga Toxins—From Cell Biology to Biomedical Applications*, Nat. Rev. Microbiol. **8**, 105 (2010).

[43] Y. X. Shen, P. O. Saboe, I. T. Sines, M. Erbakan, and M. Kumar, *Biomimetic Membranes: A Review*, J. Membr. Sci. **454**, 359 (2014).

[44] I. Medalsy, U. Hensen, and D. J. Muller, *Imaging and Quantifying Chemical and Physical Properties of Native Proteins at Molecular Resolution by Force-Volume AFM*, Angew. Chem. Int. Ed. **50**, 12103 (2011).

[45] F. Rico, C. M. Su, and S. Scheuring, *Mechanical Mapping of Single Membrane Proteins at Submolecular Resolution*, Nano Lett. **11**, 3983 (2011).

[46] M. Saleem, S. Morlot, A. Hohendahl, J. Manzi, M. Lenz, and A. Roux, *A Balance between Membrane Elasticity and Polymerization Energy Sets the Shape of Spherical Clathrin Coats*, Nat. Commun. **6**, 6249 (2015).

[47] G. Lamour, S. Souès, and A. Hamraoui, *Interplay between Long- and Short-Range Interactions Drives Neuritogenesis on Stiff Surfaces*, J. Biomed. Mater. Res. A **99A**, 598 (2011).

[48] R. E. Ducker, M. T. Montague, and G. J. Leggett, *A Comparative Investigation of Methods for Protein Immobilization on Self-Assembled Monolayers Using Glutaraldehyde, Carbodiimide, and Anhydride Reagents*, Biointerphases **3**, 59 (2008).

[49] J. E. Sader, J. W. M. Chon, and P. Mulvaney, *Calibration of Rectangular Atomic Force Microscope Cantilevers*, Rev. Sci. Instrum. **70**, 3967 (1999).

[50] K. Carvalho, J. Lemiere, F. Faqir, J. Manzi, L. Blanchoin, J. Plastino, T. Betz, and C. Sykes, *Actin Polymerization or Myosin Contraction: Two Ways to Build Up Cortical Tension for Symmetry Breaking*, Phil. Trans. R. Soc. B **368**, 20130005 (2013).

[51] S. Palmgren, P. J. Ojala, M. A. Wear, J. A. Cooper, and P. Lappalainen, *Interactions with PIP2, ADP-Actin Monomers, and Capping Protein Regulate the Activity and Localization of Yeast Twinfilin*, J. Cell Biol. **155**, 251 (2001).

[52] W. Helfrich, *Elastic Properties of Lipid Bilayers: Theory and Possible Experiments*, Z. Naturforsch. C **28**, 693 (1973).